

Efficiency-optimized near-field thermophotovoltaics using InAs and InAsSbP

F

Cite as: Appl. Phys. Lett. **121**, 193903 (2022); <https://doi.org/10.1063/5.0116806>

Submitted: 29 July 2022 • Accepted: 23 October 2022 • Published Online: 10 November 2022

 Gavin P. Forcade,  Christopher E. Valdivia,  Sean Molesky, et al.

COLLECTIONS

Note: This paper is part of the APL Special Collection on Thermal Radiation at the Nanoscale and Applications.

 This paper was selected as Featured



View Online



Export Citation



CrossMark





240 Series Sensor Input Modules

For precision cryogenic temperature monitoring over PLC networks [LEARN MORE](#) 

Efficiency-optimized near-field thermophotovoltaics using InAs and InAsSbP

Cite as: Appl. Phys. Lett. **121**, 193903 (2022); doi: [10.1063/5.0116806](https://doi.org/10.1063/5.0116806)

Submitted: 29 July 2022 · Accepted: 23 October 2022 ·

Published Online: 10 November 2022



View Online



Export Citation



CrossMark

Gavin P. Forcade,^{1,a)}  Christopher E. Valdivia,²  Sean Molesky,^{3,4}  Shengyuan Lu,⁵ Alejandro W. Rodriguez,³ Jacob J. Krich,¹  Raphael St-Gelais,⁶  and Karin Hinzer² 

AFFILIATIONS

¹Department of Physics, University of Ottawa, Ottawa, Ontario K1N 1K5, Canada

²SUNLAB, School of Electrical Engineering and Computer Science, University of Ottawa, Ottawa, Ontario K1N 1K5, Canada

³Department of Electrical and Computer Engineering, Princeton University, Princeton, New Jersey 08544, USA

⁴Department of Engineering Physics, Polytechnique Montreal, Montreal, Quebec H3T 1J4, Canada

⁵Department of Physics, Princeton University, Princeton, New Jersey 08544, USA

⁶Department of Mechanical Engineering, University of Ottawa, Ottawa, Ontario K1N 1K5, Canada

Note: This paper is part of the APL Special Collection on Thermal Radiation at the Nanoscale and Applications.

a) Author to whom correspondence should be addressed: gforc034@uottawa.ca

ABSTRACT

Waste heat is a free and abundant energy source, with 15% of global total energy use existing as waste heat above 600 K. For 600–900 K temperature range, near-field thermophotovoltaics (NFTPVs) are theorized to be the most effective technology to recycle waste heat into electrical power. However, to date, experimental efficiencies have not exceeded 1.5%. In this work, we optimize the efficiency of three modeled InAs/InAsSbP-based room-temperature NFTPV devices positioned 0.1 μm from a 750 K p-doped Si radiator. We couple a one-dimensional fluctuational electrodynamics model for the near field optics to a two-dimensional drift-diffusion model, which we validated by reproducing measured dark current–voltage curves of two previously published InAs and InAsSbP devices. The optimized devices show four to six times higher above-bandgap energy transfer compared to the blackbody radiative limit, yielding enhanced power density, while simultaneously lowering parasitic sub-bandgap energy transfer by factors of 0.68–0.85. Substituting InAs front- and back-surface field layers with InAsSbP show 1.5- and 1.4-times higher efficiency and power output, respectively, from lowered parasitic diffusion currents. Of our three optimized designs, the best performing device has a double heterostructure with an n–i–p doping order from front to back. For radiator-thermophotovoltaic gaps of 0.01–10 μm and radiators within 600–900 K, this device has a maximum efficiency of 14.2% and a maximum power output of 1.55 W/cm^2 , both at 900 K. Within 600–900 K, the efficiency is always higher with near- vs far-field illumination; we calculate up to 3.7- and 107-times higher efficiency and power output, respectively, using near-field heat transfer.

© 2022 Author(s). All article content, except where otherwise noted, is licensed under a Creative Commons Attribution (CC BY) license (<http://creativecommons.org/licenses/by/4.0/>). <https://doi.org/10.1063/5.0116806>

Waste heat above 600 K represents 15% of global total energy use,¹ and recycling this waste heat to electrical power with solid-state modules could be a general solution to improve energy-use efficiency. For 600–900 K heat sources, existing commercial waste-heat-to-electricity solid-state converters, thermoelectric generators (TEGs), have high power densities of 2 W/cm^2 but suffer from low efficiencies less than 12%.² Conversely, thermophotovoltaic (TPV) systems have high theoretical efficiencies up to 45% but low power densities of 0.2 W/cm^2 .³ Near-field thermophotovoltaic (NFTPV) systems, which position a heat source (radiator) and a TPV cell in extreme proximity, present both high theoretical efficiency and power density, up to 40%

and 10 W/cm^2 for practical devices.^{3,4} Although NFTPV systems with cells operating at room temperature have experimentally achieved 40-fold increases in power density over TPV systems,⁵ they have not exceeded 1.5% efficiency for 600–900 K radiator temperatures. This low efficiency is due to the use of TPV cells that were not optimized for near-field operation^{5,6} or InGaAs-based cells with larger-than-optimal bandgaps (0.73 eV at 300 K).^{7,8} Conversely, Lucchesi *et al.* designed a low bandgap (0.23 eV at 77 K) InSb-based NFTPV cell that was cooled to 77 K and measured a 14% efficiency with a power density of 0.75 W/cm^2 with a 732 K radiator.⁹ Although they reached a high efficiency, these cells only function properly

when cooled to cryogenic temperatures, making them impractical for most situations.

Although the spectral characteristics required for high performance in NFTPV systems are well known,^{4,10–26} concurrent optimization of the interrelated optical and electronic properties of NFTPV systems remains largely unexplored. Prior studies have not solved the full two-dimensional (2D) drift-diffusion equations in the cell, although such simulation allows realistic representation of both lateral and vertical current flow and carrier collection and is industry-standard in many other contexts.^{27–30} Many studies calculated NFTPV electrical performance using detailed balance analysis, assuming radiative recombination loss only^{10,19–22} or also including nonradiative recombination mechanisms.^{4,23–26} Other analyses have employed the diode equation with a saturation current calculated using experimentally measured lifetimes of the studied materials.^{21–28} An improved electrical model, solving the drift-diffusion equations in the low injection limit, was also employed to analyze NFTPV performance.^{31–35} Recently, studies have solved the full 1D drift-diffusion equations,^{36–39} which leads to more realistic results,³⁶ though still without lateral transport effects.

In the present work, we investigate the performance of NFTPV cells based on InAs, which has an ideal bandgap (0.353 eV at 300 K) for 600–900 K radiator temperatures and proven room temperature operating performance.^{40–46} We optimize the coupled electrical and optical properties of three NFTPV designs, all with back reflectors and two with InAs/InAsSbP double-heterostructures, by maximizing their efficiency under the illumination of a 750 K p-doped Si radiator separated by 0.1 μm . We compare their performances to a baseline design on a 500 μm substrate, shown in Fig. 1(a). We further investigate the performance for the highest-efficiency design for radiator temperatures from 600 to 900 K and with radiator-TPV gaps from 0.01 to 10 μm .

We propose three designs, presented in Figs. 1(b)–1(d). The pin and pin-Q cell designs have a p–i–n doping order from top to bottom. Conversely, the nip-Q design reverses this order to reduce lateral sheet resistance in the front-surface field (FSF) layer since electron mobilities are higher than hole mobilities (see Sec. 1 of the [supplementary material](#)). The pin-Q and nip-Q designs include the quaternary (Q) $\text{InAs}_x\text{Sb}_{0.31(1-x)}\text{P}_{0.69(1-x)}$ lattice matched to InAs with bandgap up to 0.495 eV at 300 K⁴⁷ in the FSF and base layers to reduce undesirable diffusion currents, but at the cost of higher growth complexity. All cells have a uniform temperature of 300 K (see Sec. 2 of the [supplementary material](#)) and are illuminated by high-temperature $5 \times 10^{18} \text{ cm}^{-3}$ p-type silicon radiators, separated by vacuum. The distance between gridlines is d_{G-G} while the distance between the bottom of the radiator and the top of the FSF layer is d_{R-FSF} . For comparison, we consider the baseline design [Fig. 1(a)], which is based on the fabricated TPV cell from Lu *et al.*⁴⁰ In contrast to the baseline design, we added cap and back-surface field (BSF) layers to each new design to minimize contact resistance^{48–50} and reduce undesirable minority diffusion currents. In addition, our three proposed designs have their substrates removed, increasing fabrication complexity but minimizing parasitic sub-bandgap (SBG) photon absorption. Substrate-less devices with a back reflector (BR) layer reflect SBG photons for re-absorption within the radiator, increasing efficiency, and decreasing cooling requirements for the TPV cell.

Our coupled optoelectronic model simulates the radiative thermal transport and the electrical response of the NFTPV device by combining the results of two software packages. We model radiation transport using a custom fluctuational electrodynamics solver^{51,52} that treats the devices as laterally infinite layered structures. We compute depth- and frequency-resolved radiation transfer, separated by the physical absorption mechanism, allowing us to calculate the depth-resolved electron-hole generation rate from interband absorption and

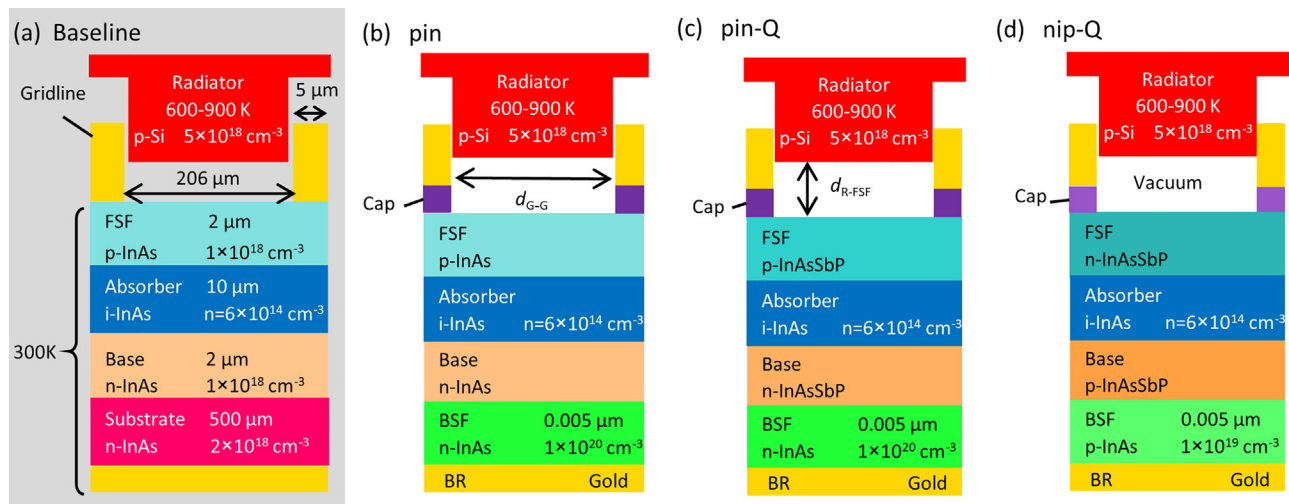


FIG. 1. Schematic diagrams of NFTPV devices: (a) TPV cell from Ref. 40 and (b)–(d) our new NFTPV designs, starting from the simplest growth of InAs only (b), then increasing performance by adding the quaternary InAsSbP [(c) and (d)]. The baseline design (a) from Ref. 40 is intended for far-field TPV and is used here for baseline comparison and simulation validation. All designs have vacuum separating the radiator and TPV cell, equal gridline widths (5 μm), and 300 K cells. Cap layer thickness is 0.02 μm and composed of (b) and (c) n-InAs doped at $1 \times 10^{20} \text{ cm}^{-3}$ and (d) p-InAs doped at $1 \times 10^{19} \text{ cm}^{-3}$. Structural parameters not given in figure for designs [(b)–(d)] are optimized with the results in Table I.

total heat transfer from lattice, free-carrier, and interband processes (see Sec. 3 of the [supplementary material](#) for model details). We verify the optical model by reproducing the spectral absorption calculated in Ref. 8; the results are shown in Sec. 4 of the [supplementary material](#).

We model the electrical transport for the NFTPV device using Synopsys TCAD Sentaurus. This software solves Poisson's equation coupled with electron and hole drift and diffusion equations to determine the TPV cell current-voltage curves as well as depth-resolved recombination rate profiles including radiative, Auger, Shockley-Read-Hall (SRH), and surface recombinations.²⁷ We apply the 1D electron-hole pair generation rate profiles, extracted from the optical model, uniformly across the illuminated portion of the 2D TPV cell, with no generation directly below the top contacts. We assume no contact and sheet resistance for both top and bottom electrodes, as they can be designed to be negligible.^{48–50} We calculate radiative and Auger recombination coefficients following the method in Ref. 53, providing Auger coefficients for InAs ($C_n = 0.48 \times 10^{-26}$ and $C_p = 1.01 \times 10^{-26}$ cm⁶/s) within the experimental uncertainties of Ref. 54. We employ a constant SRH lifetime (3.7×10^{-7} s) for both n- and p-type InAs, which provided the best fit to the measured dark-I-V curve of the TPV cell from Ref. 40. Subtracting Auger and radiative contributions from the total lifetime of Ref. 55 using Matthiessen's rule, we estimate the SRH lifetime of InAs_xSb_{0.31(1-x)}P_{0.69(1-x)} for $x \neq 1$ to be 3.2×10^{-8} s. We include a doping-dependent surface recombination velocity at the vacuum/FSF interface, discussed further in Sec. 5 of the [supplementary material](#). Due to the low conduction band density of states of InAs and InAsSbP lattice matched to InAs, we use a non-parabolic band model to calculate the electron quasi-Fermi level.⁵⁶ We employ the model and parameters from Ref. 57 to calculate the bandgap and electron affinity for all stoichiometric compositions of InAsSbP. The energy band diagrams of baseline and optimized nip-Q cells at maximum power point voltage (V_{mpp}) are presented in Fig. 2, including conduction band (E_C) and valence band (E_V) edges and the Fermi levels of electrons (E_{Fe}) and holes (E_{Fh}). Figure 2(b) shows abrupt band offsets at the heterojunctions with the FSF and BSF layers, which effectively block parasitic hole and electron transport,

respectively. We validate the electrical model, comparing measured and simulated dark current-voltage curves of p-i-n InAs⁴⁰ and p-InAsSbP/n-InAs/n⁺-InAs⁴¹ devices, with the results given in Sec. 6 of the [supplementary material](#).

With a goal to efficiently recover 600–900 K waste heat while considering achievable radiator-TPV gaps (d_{R-FSF}) of present NFTPV devices,^{5–9,58} we optimize the three NFTPV designs of Figs. 1(b)–1(d) for a radiator temperature of 750 K and $d_{R-FSF} = 0.1 \mu\text{m}$. We calculate the total optical power density absorbed by the TPV cell (P_{in}) and its maximum power point density (P_{mpp}), with power densities defined as power divided by the illuminated area. We then optimize the device structure to maximize device efficiency, $\eta = P_{mpp}/P_{in}$, using an iterative optimizer with parameter domain sampling defined by the face-centered central composite method.⁵⁹ We optimize for efficiency as opposed to power as it increases waste heat use while also lowering cell cooling requirements.

To speed up the optimization, we hold constant the parameters with fixed values listed in Fig. 1. This includes the cap and BSF layer doping concentrations, which are set at readily achievable values^{48–50} to maximize current collection and quench contact resistance. This choice necessitates a thin BSF layer to minimize free-carrier absorption. We employ an intrinsic InAs absorber layer to maximize absorption³¹ while minimizing the Auger recombination that dominates in cells using p-InAs.⁴⁰ See Sec. 7 of the [supplementary material](#) for effects of varying Cap and BSF layer thickness and doping on performance.

We consider the radiator to be semi-infinite, but instead using a 500- μm thickness decreases total radiation transfer by less than 1%. A separate optimization showed that our chosen radiator doping of 5×10^{18} cm⁻³ maximizes above-bandgap (ABG) radiation transfer for realistic radiator thicknesses (on the order of a typical 500 μm Si substrate or less). Thinner radiators demand higher doping concentrations to maximize ABG radiation transfer, but such radiators also increase SBG radiation transfer, which hurts efficiency.

Layer thicknesses and doping not specified in Fig. 1 are included as parameters for optimization. The optimization domain and results for all designs illuminated by a 750 K radiator with $d_{R-FSF} = 0.1 \mu\text{m}$ are

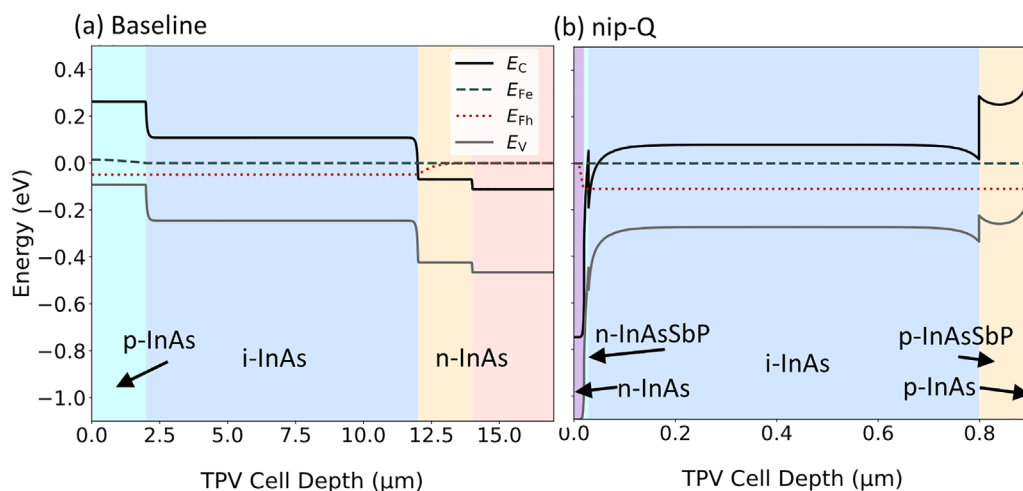


FIG. 2. Band diagram, with cutline through the top contact, at maximum power point voltage (V_{mpp}) of the (a) baseline and (b) optimized nip-Q TPV cells, illuminated by a 750 K radiator with $d_{R-FSF} = 0.1 \mu\text{m}$. Note the different horizontal scales.

TABLE I. Optimized NFTPV cell structure for a 750 K p-Si radiator and $d_{R-FSF} = 0.1 \mu\text{m}$, with their optimization bounds and performance metrics.

	Parameter	Units	Range	Baseline ^a	pin	pin-Q	nip-Q
Input	d_{G-G}	μm	20–300	206	49	49	78
	FSF thickness	μm	0.005–2.0	2.0	0.0053	1.1	0.0089
	FSF $\text{InAs}_x\text{Sb}_{0.31(1-x)}\text{P}_{0.69(1-x)}$		$x = 0.4–1.0$	1.0	1.0 ^a	0.4	0.46
	FSF doping	cm^{-3}	$6 \times 10^{14}–10^{19}$	$p = 10^{18}$	$p = 10^{19}$	$p = 2 \times 10^{17}$	$n = 4 \times 10^{15}$
	Absorber thickness	μm	0.1–3.0	10.0	0.72	0.77	0.77
	Base thickness	μm	0.005–2.0	2.0	0.062	0.055	0.10
	Base $\text{InAs}_x\text{Sb}_{0.31(1-x)}\text{P}_{0.69(1-x)}$		$x = 0.4–1.0$	1.0	1.0 ^a	0.76	0.4
Output	Base doping	cm^{-3}	$6 \times 10^{14}–10^{19}$	$n = 10^{18}$	$n = 6 \times 10^{14}$	$n = 7 \times 10^{16}$	$p = 2 \times 10^{15}$
	J_{sc}	A cm^{-2}	...	1.75	2.39	2.46	2.36
	V_{oc}	V	...	0.065	0.108	0.143	0.145
	P_{mpp}	mW cm^{-2}	...	34	121	204	203
	η	%	...	0.29	4.8	8.0	9.0

^aFixed at a given value.

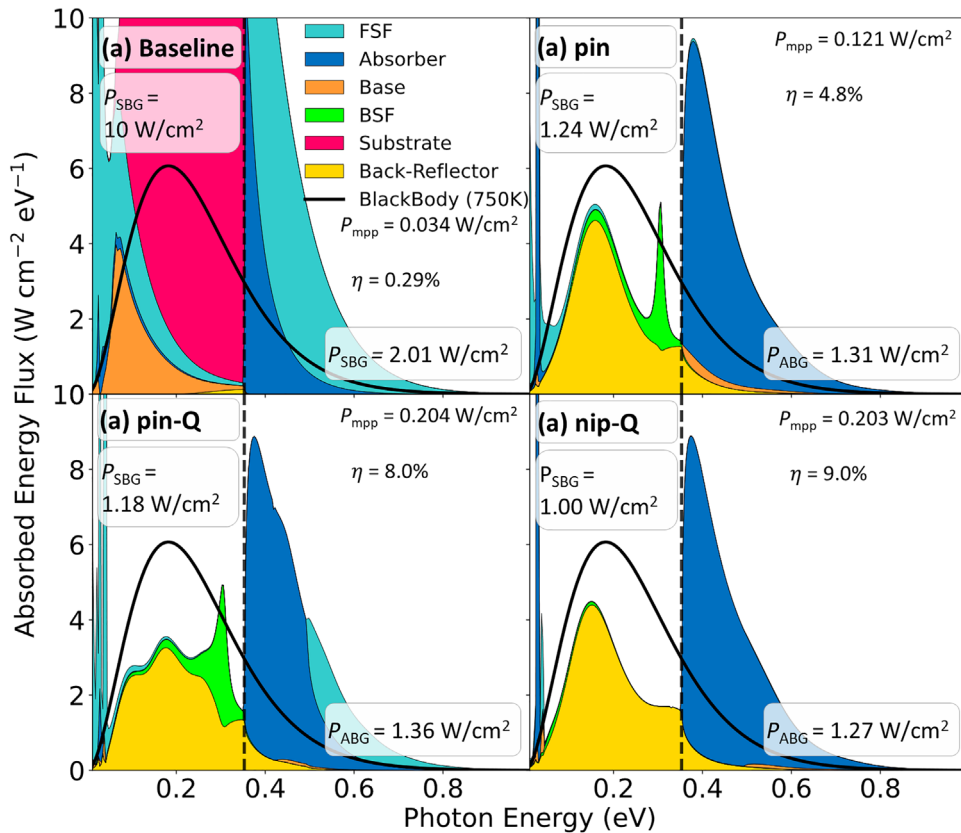


FIG. 3. Spectral absorption distribution within NFTPV cell layers for a 750 K radiator and $d_{R-FSF} = 0.1 \mu\text{m}$, for designs: (a) baseline and optimized (b) pin, (c) pin-Q, and (d) nip-Q. Solid black line represents the blackbody radiative limit at 750 K. The vertical dashed lines represent the bandgap of InAs, which separates parasitic sub-bandgap (SBG) and useful above-bandgap (ABG) absorption, respectively. We include total SBG and ABG absorbed power, P_{SBG} and P_{ABG} , respectively.

given in Table I. The optimized As mole fraction (x) of $\text{InAs}_x\text{Sb}_{0.31(1-x)}\text{P}_{0.69(1-x)}$, for the FSF and base layers of the pin-Q and nip-Q designs, respectively, reached the lower bound of 0.4, which we constrained to high quality compositions^{60,61} outside the miscibility gap.⁶² The p-type doping concentration for the FSF layer of the pin design reached the upper bound of 10^{19} cm^{-3} , which we limited to readily achievable concentrations for these devices.^{49–51} These bounded values minimize parasitic electron diffusion; the lower bound Q has the largest bandgap with favorable band-alignment as a p-type material (see Fig. 2) while the pin design requires high p-doping to perform the same task.

The FSF conductivity effects can only be captured with 2+ dimension drift-diffusion solvers, highlighting the importance of our electrical model. To minimize lateral series resistance, the p-type FSF layer must be thick and moderately doped (pin-Q) or thin and highly doped (pin). The n-type FSF layer of the nip-Q device further reduces top sheet resistance, since electron mobility is higher than hole mobility, allowing for a thin and moderately doped FSF layer with 60% larger d_{G-G} , increasing power output density.

Comparing parameters of the optimized designs to the baseline design, the optimized designs have smaller d_{G-G} values and are

composed of much thinner layers. Thinner cells improve device performance due to higher carrier collection efficiency and lower parasitic free carrier absorption but reduce current generation. However, the thin designs have higher J_{sc} than the baseline due to shorter penetration depth of evanescent vs propagating waves and high reflection at the gold BR layer. The base layers optimally reached lower doping concentrations to reduce SBG power transfer (P_{SBG}) originating from free-carrier absorption.

Our optical model calculates a significant enhancement of useful ABG power transfer (P_{ABG}) over the blackbody radiative limit for all devices. Figure 3 shows the layer-resolved spectral absorbed energy flux for each device. A 750 K blackbody radiative spectrum represented by the solid black line is included for comparison, along with a vertical dashed black line denoting the bandgap of InAs (0.353 eV). The optimized devices have P_{SBG} approximately 10% of that in the baseline design. P_{SBG} is not converted to useful power and instead raises the TPV cooling requirements. P_{SBG} could be further reduced with a more reflective BR.^{16,63} The optimized designs [Figs. 3(b)–3(d)] have 4–6 times higher total P_{ABG} and 0.68–0.85 times lower P_{SBG} compared to the blackbody limit. Although P_{ABG} of the efficiency-optimized designs are about 70% of the baseline design, we see much

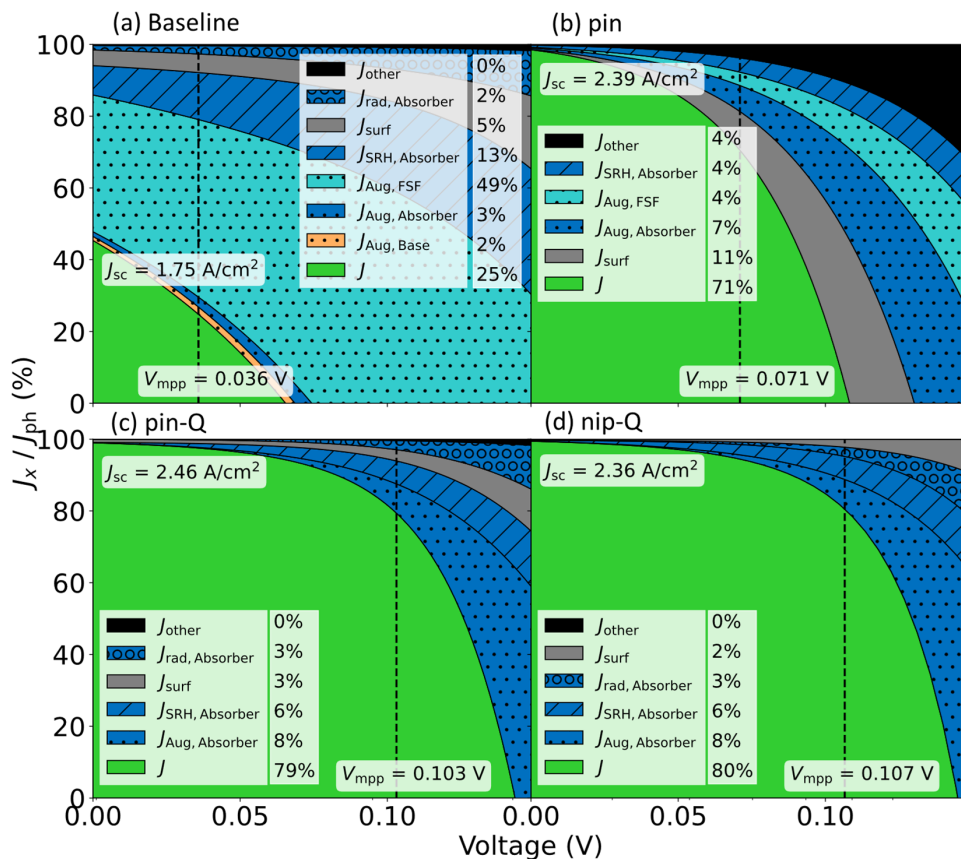


FIG. 4. Current–voltage curves of extracted (J) and region-resolved recombination currents (J_x) normalized to the total photogenerated current (J_{ph}) for a 750 K radiator and $d_{R-FSF} = 0.1 \mu\text{m}$ for designs: (a) baseline, (b) pin, (c) pin-Q, and (d) nip-Q. The vertical dashed lines show V_{mpp} operation of the devices. Current recombination types are stacked from largest to smallest contributor at V_{mpp} , which are then stacked following the cell structure. Currents that account for less than 1.5% of J_{ph} at V_{mpp} are lumped in J_{other} . Current contributions at V_{mpp} are provided in the legend.

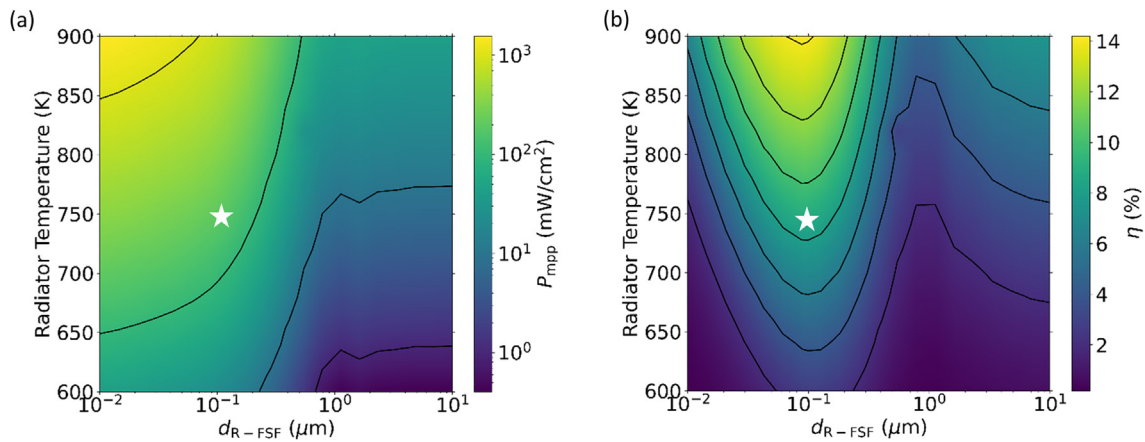


FIG. 5. (a) Power output and (b) efficiency of our optimized nip-Q device as a function of radiator temperature and radiator-TPV gap. Stars depict parameters used for device optimization.

higher efficiency and power output (Table I) due to order-of-magnitude thinner absorption layers, which improves current collection.

Up to 80% of available current is collected at V_{mpp} for the optimized designs compared to just 39% for the baseline, highlighting the importance of optimizing electronic device properties for near-field operation. Figure 4 shows the current-voltage characteristics, normalized to the total photo-generated current (J_{ph}), of the four designs. We include extracted current (J), surface recombination at the vacuum/FSF and electrode/semiconductor interfaces (J_{surf}), as well as Auger ($J_{\text{Aug},l}$), radiative ($J_{\text{rad},l}$), and Shockley-Read-Hall ($J_{\text{SRH},l}$) recombination currents in layer l . All currents that contribute less than 1.5% to J_{ph} at V_{mpp} are combined into J_{other} . Auger recombination is the main electrical loss mechanism for all designs, consuming 8%–54% of J_{ph} at V_{mpp} . However, the devices could be further improved using higher quality absorber layer material, i.e., lowering SRH recombination. Comparing Figs. 4(b) and 4(c), we find that the introduction of the quaternary InAsSbP in the FSF and base layers reduces surface recombination by two-third and eliminates recombination in all but the absorber layer, contributing to a 45% larger V_{mpp} . Designs with InAsSbP, nip-Q and pin-Q, have similar normalized current-voltage characteristics [see Figs. 4(c) and 4(d)]; therefore, nip-Q's performance enhancement (Table I) is due to better P_{SBG} management and larger $d_{\text{G-G}}$.

Using our best design, the optimized nip-Q device, we explore the impact of radiator temperature and $d_{\text{R-FSF}}$ on the power output and efficiency in Fig. 5. The star represents the parameter values used during the nip-Q device optimization. We calculate a significant power output enhancement from near-field energy transfer for all radiator temperatures investigated, with the largest enhancement being 107-fold larger than the far-field ($d_{\text{R-FSF}} = 10 \mu\text{m}$), occurring with $d_{\text{R-FSF}} = 0.01 \mu\text{m}$ and a 600 K radiator. We also calculate an improved efficiency under near-field illumination for all radiator temperatures within 600–900 K, reaching up to a 3.7-fold increase with a 600 K radiator and $d_{\text{R-FSF}} = 0.12 \mu\text{m}$ compared to a far-field device.

The maximum efficiency for a given radiator temperature varies with $d_{\text{R-FSF}}$. The optimal $d_{\text{R-FSF}}$ decreases as temperature increases, going from 0.12 to 0.09 μm for a 600–900 K radiator, respectively. This shift toward smaller $d_{\text{R-FSF}}$ occurs because there is proportionally less

near-field P_{SBG} transfer to the FSF layer for higher radiator temperatures. Finally, the dip in efficiency at $d_{\text{R-FSF}} \approx 1 \mu\text{m}$ is caused by a lowered P_{ABG} relative to P_{SBG} due to propagative wave interference effects. Since the relative fraction of P_{ABG} vs P_{SBG} increases with radiator temperature, the highest efficiency and power output of 14.2% and $1.55 \text{ W}/\text{cm}^2$ occur at 900 K. P_{ABG} increases as $d_{\text{R-FSF}}$ decreases, but P_{SBG} absorbed in the FSF layer also increases rapidly below 0.1 μm , which reduces efficiency without impacting power output. Therefore, the maximum efficiency and power output occur at different $d_{\text{R-FSF}}$ of 0.09 and 0.01 μm (lower limit), respectively.

Simulation of our optimized nip-Q design significantly outperforms the simulated p-InAs/n-InAs design studied in Ref. 31. At 800 K and with $d_{\text{R-FSF}} = 0.1 \mu\text{m}$, we calculate approximately 2.7- and 3.3-times higher efficiency and power density relative to that device (compared to their efficiency that assumes no absorption in the substrate). The nip-Q device performance enhancement is attributed to our BR layer, use of Q material, and n-i-p doping configuration.

In summary, three NFTPV cell designs containing InAs and/or InAsSbP were optimized and compared under near-field illumination by a 750 K p-Si radiator at $d_{\text{R-FSF}} = 0.1 \mu\text{m}$, using a validated optoelectronic model solving full 2D drift-diffusion equations and fluctuation electrodynamics. The optimized devices have 4–6 times higher above-bandgap and 0.68–0.85 times less sub-bandgap radiation transfer than the blackbody limit. Over the 600–900 K radiator temperature range, we calculate up to 14.2% efficiency and $1.55 \text{ W}/\text{cm}^2$ power output for the best performing device design. According to these results, our best design could significantly outperform the best measured NFTPV device for the conversion of 600–900 K waste heat, providing important guidelines for the design of future NFTPV cells.

See the [supplementary material](#) for further details and validation of the optical and electrical model, the calculated temperature gradient of the device, and the impact on device performance of parameters that were fixed during optimization.

The authors thank University of Ottawa colleagues C. Zhang and M. Giroux for discussions on this topic. This work was supported in part by the Natural Sciences and Engineering

Research Council of Canada (No. NSERC CGS-D) and by the New Frontiers in Research Fund (No. NFRFE-2019-00334). They are also grateful to CMC Microsystems for providing access to the Synopsys Sentaurus software (vS-2021.06).

AUTHOR DECLARATIONS

Conflict of Interest

The authors have no conflicts to disclose.

Author Contributions

Gavin Paul Forcade: Data curation (lead); Formal analysis (lead); Funding acquisition (supporting); Investigation (lead); Methodology (lead); Software (equal); Validation (lead); Visualization (lead); Writing – original draft (lead); Writing – review & editing (lead). **Christopher E. Valdivia:** Funding acquisition (supporting); Supervision (equal); Writing – review & editing (equal). **Sean Molesky:** Methodology (supporting); Software (equal); Supervision (supporting); Writing – review & editing (supporting). **Shengyuan Lu:** Investigation (supporting); Software (supporting); Validation (supporting). **Alejandro Rodriguez:** Conceptualization (equal); Funding acquisition (supporting); Software (supporting); Writing – review & editing (supporting). **Jacob J Krich:** Methodology (supporting); Software (equal); Supervision (supporting); Writing – review & editing (equal). **Raphael St-Gelais:** Conceptualization (lead); Funding acquisition (lead); Investigation (supporting); Software (supporting); Supervision (supporting); Writing – review & editing (supporting). **Karin Hinzer:** Conceptualization (equal); Funding acquisition (supporting); Resources (equal); Supervision (lead); Writing – review & editing (supporting).

DATA AVAILABILITY

The data that support the findings of this study are available from the corresponding author upon reasonable request.

REFERENCES

- ¹C. Forman, I. K. Muritala, R. Pardemann, and B. Meyer, *Renewable Sustainable Energy Rev.* **57**, 1568 (2016).
- ²See <https://thermoelectric-generator.com/> for thermoelectric generators (2022).
- ³I. A. Okanimba Tedah, F. Maculewicz, D. E. Wolf, R. Schmechel, I. A. O. Tedah, F. Maculewicz, D. E. Wolf, and R. Schmechel, *J. Phys. D: Appl. Phys.* **52**, 275501 (2019).
- ⁴B. Zhao, K. Chen, S. Buddhiraju, G. Bhatt, M. Lipson, and S. Fan, *Nano Energy* **41**, 344 (2017).
- ⁵A. Fiorino, L. Zhu, D. Thompson, R. Mittapally, P. Reddy, and E. Meyhofer, *Nat. Nanotechnol.* **13**, 806 (2018).
- ⁶G. R. Bhatt, B. Zhao, S. Roberts, I. Datta, A. Mohanty, T. Lin, J. M. Hartmann, R. St-Gelais, S. Fan, and M. Lipson, *Nat. Commun.* **11**, 2545 (2020).
- ⁷T. Inoue, T. Koyama, D. D. Kang, K. Ikeda, T. Asano, and S. Noda, *Nano Lett.* **19**, 3948 (2019).
- ⁸R. Mittapally, B. Lee, L. Zhu, A. Reihani, J. W. Lim, D. Fan, S. R. Forrest, P. Reddy, and E. Meyhofer, *Nat. Commun.* **12**, 4364 (2021).
- ⁹C. Lucchesi, D. Cakiroglu, J. P. Perez, T. Talierno, E. Tournié, P. O. Chapuis, and R. Vaillon, *Nano Lett.* **21**, 4524 (2021).
- ¹⁰W. Shen, J. Xiao, Y. Wang, S. Su, J. Guo, and J. Chen, *J. Appl. Phys.* **128**, 035105 (2020).
- ¹¹M. D. Whale and E. G. Cravalho, *IEEE Trans. Energy Convers.* **17**, 130 (2002).
- ¹²J. I. Watjen, X. L. Liu, B. Zhao, and Z. M. Zhang, *J. Heat Transfer* **139**, 052704 (2017).

- ¹³M. Laroche, R. Carminati, and J. J. Greffet, *J. Appl. Phys.* **100**, 063704 (2006).
- ¹⁴K. Park, S. Basu, W. P. King, and Z. M. Zhang, *J. Quant. Spectrosc. Radiat. Transfer* **109**, 305 (2008).
- ¹⁵Q. Cai, P. Chen, S. Cao, Q. Ye, and X. Wu, *Int. J. Thermophys.* **41**, 161 (2020).
- ¹⁶T. Inoue, T. Suzuki, K. Ikeda, T. Asano, and S. Noda, *Opt. Express* **29**, 11133 (2021).
- ¹⁷R. Wang, J. Lu, and J. H. Jiang, *Chin. Phys. Lett.* **38**, 024201 (2021).
- ¹⁸J. Song, M. Lim, S. S. Lee, and B. J. Lee, *Phys. Rev. Appl.* **11**, 44040 (2019).
- ¹⁹T. Inoue, K. Watanabe, T. Asano, and S. Noda, *Opt. Express* **26**, A192 (2018).
- ²⁰B. Wang, C. Lin, and K. H. Teo, *J. Photonics Energy* **7**, 044501 (2017).
- ²¹H. Yu, D. Liu, Y. Duan, and Z. Yang, *J. Quant. Spectrosc. Radiat. Transfer* **217**, 235 (2018).
- ²²A. Karalis and J. D. Joannopoulos, *Sci. Rep.* **6**, 22270 (2016).
- ²³G. T. Papadakis, S. Buddhiraju, Z. Zhao, B. Zhao, and S. Fan, *Nano Lett.* **20**, 1654 (2020).
- ²⁴T. Liao, X. Zhang, X. Chen, and J. Chen, *J. Appl. Phys.* **125**, 203103 (2019).
- ²⁵T. Liao, Z. Yang, W. Peng, X. Chen, and J. Chen, *Energy Convers. Manag.* **152**, 214 (2017).
- ²⁶B. Zhao, P. Santhanam, K. Chen, S. Buddhiraju, and S. Fan, *Nano Lett.* **18**, 5224 (2018).
- ²⁷M. M. Wilkins and K. Hinzer, *Handbook of Optoelectronic Device Modeling and Simulation* (CRC Press, 2017).
- ²⁸M. Wilkins, C. E. Valdivia, and A. M. Gabr, *J. Appl. Phys.* **118**, 143102 (2015).
- ²⁹C.-K. Li and Y.-R. Wu, *IEEE Trans. Electron Devices* **59**, 2 (2012).
- ³⁰E. M. Tonita, C. E. Valdivia, M. Martinez-Szewczyk, M. R. Lewis, M. I. Bertoni, and K. Hinzer, *Sol. Energy Mater. Sol. Cells* **230**, 111293 (2021).
- ³¹D. Milovich, J. Villa, E. Antolin, A. Datas, A. Marti, R. Vaillon, and M. Francoeur, *J. Photonics Energy* **10**, 025503 (2020).
- ³²A. Datas and R. Vaillon, *Appl. Phys. Lett.* **114**, 133501 (2019).
- ³³M. Lim, J. Song, J. Kim, S. S. Lee, I. Lee, and B. J. Lee, *J. Quant. Spectrosc. Radiat. Transfer* **210**, 35 (2018).
- ³⁴R. Vaillon, J.-P. Pérez, C. Lucchesi, D. Cakiroglu, P.-O. Chapuis, T. Talierno, and E. Tournié, *Opt. Express* **27**, A11 (2019).
- ³⁵J. Legendre and P. O. Chapuis, *Sol. Energy Mater. Sol. Cells* **238**, 111594 (2022).
- ³⁶E. Blandre, P.-O. Chapuis, and R. Vaillon, *Sci. Rep.* **7**, 15860 (2017).
- ³⁷D. Feng, E. J. Tervo, D. Vasilevska, S. K. Yee, A. Rohatgi, and Z. M. Zhang, *J. Appl. Phys.* **129**, 213101 (2021).
- ³⁸D. Feng, S. K. Yee, and Z. M. Zhang, *Sol. Energy Mater. Sol. Cells* **237**, 111562 (2022).
- ³⁹W. A. Callahan, D. Feng, Z. M. Zhang, E. S. Toberer, A. J. Ferguson, and E. J. Tervo, *Phys. Rev. Appl.* **15**, 54035 (2021).
- ⁴⁰Q. Lu, X. Zhou, A. Krysa, A. Marshall, P. Carrington, C. H. Tan, and A. Krier, *Sol. Energy Mater. Sol. Cells* **179**, 334 (2018).
- ⁴¹A. Krier, M. Yin, A. Marshall, and S. E. Krier, *J. Electron. Mater.* **45**, 2826 (2016).
- ⁴²A. Krier, M. Yin, A. R. J. Marshall, M. Kesaria, S. E. Krier, S. McDougall, W. Meredith, A. D. Johnson, J. Inskip, and A. Scholes, *Infrared Phys. Technol.* **73**, 126 (2015).
- ⁴³B. A. Matveev, V. I. Ratushnyi, and A. Y. Rybal'chenko, *Tech. Phys.* **64**, 1164 (2019).
- ⁴⁴V. A. Gevorkyan, V. M. Aroutiounian, K. M. Gambaryan, I. A. Andreev, L. V. Golubev, and Y. P. Yakovlev, *Tech. Phys. Lett.* **34**, 69 (2008).
- ⁴⁵E. V. Kunitsyna, I. A. Andreev, V. V. Sherstnev, T. V. L'Vova, M. P. Mikhailova, Yu. P. Yakovlev, M. Ahmetoglu, G. Kaynak, and O. Gurler, *Opt. Mater. (Amst.)* **32**, 1573–1577 (2010).
- ⁴⁶V. P. Khvostikov, L. S. Lunin, V. V. Kuznetsov, V. I. Ratushny, V. Oliva, O. A. Khvostikova, and M. Z. Shvarts, *Tech. Phys. Lett.* **29**, 851 (2003).
- ⁴⁷S. Adachi, *Handbook on Physical Properties of Semiconductors*, 1st ed. (Springer, New York, 2017).
- ⁴⁸A. Baraskar, V. Jain, M. A. Wistey, U. Singiseti, Y. J. Lee, B. Thibeault, A. Gossard, and M. J. W. Rodwell, in *International Conference on Indium Phosphide and Related Materials* (IPRM, 2010), p. 481.
- ⁴⁹A. Katz, S. N. G. Chu, and B. E. Weir, *J. Vac. Sci. Technol. B* **8**, 1125 (1990).
- ⁵⁰W. Lu, B. R. Bennett, J. B. Boos, and J. A. Del Alamo, *Electron. Lett.* **36**, 546 (2000).

- ⁵¹M. T. H. Reid, A. W. Rodriguez, and S. G. Johnson, *Proc. IEEE* **101**, 531 (2013).
- ⁵²S. Molesky and S. Lu, “heatSlabs” (2020). <https://Github.Com/SeanMolesky/HeatSlabs>
- ⁵³A. Rogalski and Z. Orman, *Infrared Phys.* **25**, 551 (1985).
- ⁵⁴S. Marchetti, M. Martinelli, and R. Simili, *J. Phys: Condens. Matter* **14**, 3653 (2002).
- ⁵⁵G. A. Sukach, A. B. Bogoslovskaya, P. F. Oleksenko, Y. Y. Bilynets, and V. N. Kabacij, *Infrared Phys. Technol.* **41**, 299 (2000).
- ⁵⁶A. Raymond, J. L. Robert, and C. Bernard, *J. Phys. C* **12**, 2289 (1979).
- ⁵⁷M. Grigoryev, E. Ivanov, and K. Moiseev, *Semiconductors* **45**, 1334 (2011).
- ⁵⁸R. St-Gelais, L. Zhu, S. Fan, and M. Lipson, *Nat. Nanotechnol.* **11**, 515 (2016).
- ⁵⁹*Sentaurus TCAD User's Manual* (Synopsys, Inc., 2021).
- ⁶⁰I. A. Andreev, O. Y. Serebrennikova, N. D. Il'inskaya, A. A. Pivovarova, G. G. Kononov, E. V. Kunitsyna, V. V. Sherstnev, and Y. P. Yakovlev, *Semiconductors* **49**, 1671 (2015).
- ⁶¹E. Tournie, J. L. Lazzari, H. Mani, F. Pitard, C. L. Alibert, and A. F. Joullie, *Proc. SPIE* **1361**, 641 (1991).
- ⁶²I. Vurgaftman, J. R. Meyer, and L. R. Ram-Mohan, *J. Appl. Phys.* **89**, 5815 (2001).
- ⁶³D. Fan, T. Burger, S. McSherry, B. Lee, A. Lenert, and S. R. Forrest, *Nature* **586**, 237 (2020).

Efficiency-optimized near-field thermophotovoltaics using InAs and InAsSbP: Supplementary Material

1. Carrier Mobility

Both the optical and electrical models need accurate doping-dependent carrier mobilities for InAs and InAsSbP, therefore we employ the low-field doping-dependent mobility model at room temperature:¹

$$\mu(N) = \mu_{\min} + \frac{\mu_{\max} - \mu_{\min}}{1 + \left(\frac{N}{N_{\text{ref}}}\right)^{\lambda_{\mu}}} \quad (\text{S1})$$

where μ_{\min} , μ_{\max} , N_{ref} , and λ_{μ} are positive fitting parameters. To calculate the carrier mobilities of InAsSbP, we interpolate parameters between binaries, applying Matthiessen's Rule to interpolate μ_{\min} and μ_{\max} , and linear interpolation for N_{ref} and λ_{μ} . We employ fitting parameter values from Refs. 1,2 to describe both carrier mobilities for InSb and InP, and the hole mobility of InAs. For the electron mobility of InAs, we fit Eq. (S1) to experimental data from Refs. 3–8 to calculate its fitting parameters, shown in Fig. S1. For comparison, we also include the curve calculated using parameters proposed by Sotoodeh et al.¹, showing their proposed parameters are inappropriate for doping concentrations higher than $\sim 1 \times 10^{17} \text{ cm}^{-3}$. We provide our best fit values in Table S1, and compare to values from Sotoodeh et al.¹.

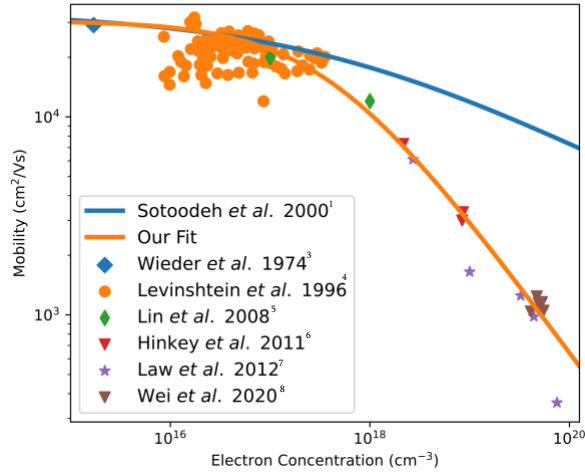


Figure S1. InAs electron mobility data as a function of electron concentration, together with the model fitting obtained by Sotoodeh et al.¹ and by this work. The experimental data are taken from Refs. 3–8.

Table S1. Parameters to describe electron mobility of InAs. We compare the parameters from our fit to parameters from Sotoodeh et al.¹

Parameters	Units	Sotoodeh et al. ¹	Our Fit
μ_{\min}	cm^2/Vs	1000	0.3
μ_{\max}	cm^2/Vs	34000	30600
N_{ref}	cm^{-3}	1.1×10^{18}	3.6×10^{17}
λ_{μ}		0.32	0.68

2. Cell temperature calculations

We assume the TPV cells are kept uniformly at 300 K. To verify this assumption, we can estimate the temperature gradient of our nip-Q design using Fourier's Law for heat conduction⁹:

$$q = -\frac{\kappa\Delta T}{L} \quad (\text{S2})$$

where κ is the room-temperature thermal conductivity ($0.3 \text{ W cm}^{-1} \text{ K}^{-1}$ for bulk InAs),¹⁰ L is the layer thickness, and ΔT is the temperature gradient between both ends of L . Figure Figure S2 depicts the temperature (relative to 300 K) through the cell for the optimized nip-Q design, illuminated by a 900 K radiator and a 10 nm radiator-cell gap. We find a maximum temperature difference of $\Delta T \sim 0.005 \text{ K}$ which has negligible effects on our optoelectronic model. This agrees with a previous study¹¹ of a similar NFTPV system: a thin film $\text{In}_{0.53}\text{Ga}_{0.47}\text{As}$ cell bonded with Parylene-C on a Silicon wafer handle, and illuminated by a 1270 K Si radiator. They calculated a maximum temperature gradient of $\Delta T \sim 1.5 \text{ K}$ for their system. Their temperature gradient is much higher than our value, albeit still negligible, and is due to the low thermal conductivity of the Parylene-C layer.

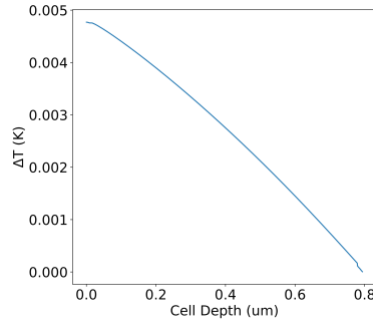


Figure S2. Depth resolved temperature, relative to 300 K, of the nip-Q cell illuminated by a 900 K radiator and a 10 nm radiator-cell gap.

3. Optical model details

The model incorporates dielectric functions of all materials for photon energies from 0.01–1 eV; heat transfer is negligible outside this range for this system. We use the temperature and doping dependent dielectric function model proposed by Fu and Zhang¹² for the Si radiator, however we replace their free-carrier concentration model with the model proposed by Basu et al.¹³ We use the temperature-dependent bandgap model of Si from Ref. 14. The dielectric function described in Ref. 15 is applied to the gold back-reflector. To model the optical properties of InAs and InAsSbP, we consider interband, lattice, and free carrier processes. To model the frequency (ω) dependent optical properties of InAs and InAsSbP, we employ the Drude-Lorentz model:^{16,17}

$$\epsilon(\omega) = \epsilon_{IB}(\omega) + \epsilon_{\infty} \left(\sum_j \frac{S_j(\omega_{LO,j}^2 - \omega_{TO,j}^2)}{\omega_{TO,j}^2 - \omega^2 - i\omega\gamma_j} - \frac{\omega_p^2}{\omega(\omega + i\Gamma)} \right) \quad (\text{S3})$$

where

$$\omega_p^2 = \frac{N_q e^2}{\epsilon_0 \epsilon_{\infty} m_q^*}, \quad \Gamma = \frac{e^2}{m_q^* \mu_q} \quad q = e, h \quad (\text{S4})$$

where e is the elementary charge, ϵ_0 is the vacuum permittivity, ϵ_{∞} is the high-frequency permittivity, m_e^* and m_h^* are the electron and hole effective masses, respectively, μ_e and μ_h are the electron and hole mobilities, respectively, N_e and N_h are the concentrations of free electrons and holes (assuming fully ionized dopants), respectively, S_j is the anion atom fraction, $\omega_{LO,j}$ and $\omega_{TO,j}$ are the longitudinal and transverse optical phonon frequencies, respectively, and γ_j is the damping constant due to phonons of the j th lattice oscillator (binary constituent). We calculate the interband contribution (ϵ_{IB}) following the method from Ref. 17 with some parameters from Ref. 18, however instead of calculating the refractive index with Kramers-Kronig relations as was done in Ref. 17, we assume $n_{IB} = \sqrt{\epsilon_{\infty}}$ to improve computational speed by approximately a factor of 13 by avoiding integrals when evaluating the dielectric function. We investigated the impact of this approximation, finding that our method underestimates the total power

transfer by approximately 1.5% compared to using the Kramers-Kronig relations for the optimized nip-Q design separated by 0.1 μm from a 750 K radiator.

With donor doping of the quaternary InAsSbP of $1 \times 10^{20} \text{ cm}^{-3}$, the Fermi level goes about 0.1 eV into the conduction band for all stoichiometric compositions of InAsSbP lattice matched to InAs. Nonparabolic corrections to the band structure then become important as well as increasing the apparent electron effective mass when describing optical properties.¹⁹ We therefore model a doping-dependent electron effective mass ($m_{e,\text{InAsSbP}}^*(N_e)$) by assuming it has the same dependence on electron concentration N_e as is observed in InAs. We find the effective mass by interpolating the effective masses of the binary compounds given in Table S2 ($m_{e,\text{InAsSbP}}^*(0)$) and add the difference between the electron effective masses of InAs from Ref. 19 ($m_{e,\text{InAs}}^*(N)$) and Table S2 ($m_{e,\text{InAs}}^*(0)$):

$$m_{e,\text{InAsSbP}}^*(N_e) = m_{e,\text{InAsSbP}}^*(0) + \left(m_{e,\text{InAs}}^*(N_e) - m_{e,\text{InAs}}^*(0) \right) \quad (\text{S5})$$

All other parameters employed in the optical model are given in Table S2. See Section 1 for further details on the carrier mobility model.

Table S2. Parameters to describe optical properties of InAs and InAsSbP, with references. m_0 is the free-electron mass.

Parameters	Units	InAs	InSb	InP	Ref
ϵ_∞		11.6	15.3	9.9	20
m_e^*	m_0	0.024	0.013	0.079	9
m_h^*	m_0	0.36	0.38	0.72	9
γ_j	10^{11} rad/s	9.23	5.41	3.58	16
$\omega_{\text{LO},j}$	10^{13} rad/s	4.55	3.59	6.52	9
$\omega_{\text{TO},j}$	10^{13} rad/s	4.14	3.38	5.74	9

4. Optical model validation

We validated the predictions of our custom optical model by reproducing the independently calculated spectral absorption of the InGaAs/InP device structure from Mittapally et al.¹¹ under a 1270 K radiator. Figure SError! Reference source not found. compares their results (dashed line) to our simulations (stack plot) for three radiator-TPV gaps, showing only minor discrepancies which are due to slight differences between dielectric functions employed. We calculate at most a 5% relative difference for both above and below bandgap power transfer compared to Ref. 11 (see Table S3). Note, for the 100 nm gap configuration, spectral data from Ref. 11 is cut-off at $30 \text{ W cm}^{-2} \text{ eV}^{-1}$ below 0.07 eV, therefore the sub bandgap power transfer within Table S3 is integrated down to 0.07 eV instead of 0 eV.

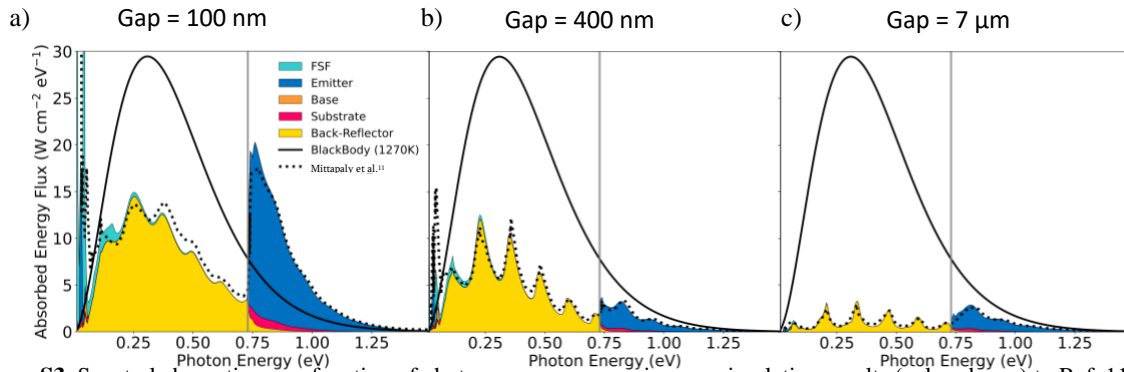


Figure S3. Spectral absorption as a function of photon energy, comparing our simulation results (colored area) to Ref. 11 (dashed line). We include an equivalent blackbody spectrum for scale (solid line). The bandgap of the absorber layer is given by the solid gray line. The three plots represent different radiator-TPV gaps: (a) 0.1 μm , (b) 0.4 μm , and (c) 7 μm .

Table S3. Comparing calculated above bandgap and sub bandgap power transfer from our simulations to results from Mittapally et al.¹¹

Power Transfer ($W\text{ cm}^{-2}$)		100 nm	400 nm	7 μm
Above bandgap	Us	3.8	0.69	0.61
	Mittapally et al. ¹¹	4.0	0.66	0.60
Sub bandgap	Us	5.9	3.7	0.67
	Mittapally et al. ¹¹	6.1	3.7	0.70

5. Surface recombination model

As surface recombination velocity can be highly dependent on doping concentration,²¹ we model the doping-dependent surface recombination velocity (S in cm/s) for the vacuum/FSF interface with the empirical function:

$$\log_{10}(S) = \frac{1}{\exp\left(\left(a - \log_{10}(N_q)\right)b\right) + c}, \quad q = D, A \quad (\text{S6})$$

where a , b , and c are fitting parameters, N_D and N_A are the donor and acceptor doping concentrations in cm^{-3} , respectively. Figure S4 shows our fit of Eq. (S6) to measured data from Refs. 22,23 and an extracted value from Table S4 of Lu et al.²⁴, yielding $a = 14.5$, $b = 2.4$, and $c = 0.19$. We apply identical values for both n- and p-type doping and for all Sb- and/or P- compositions of InAsSbP.

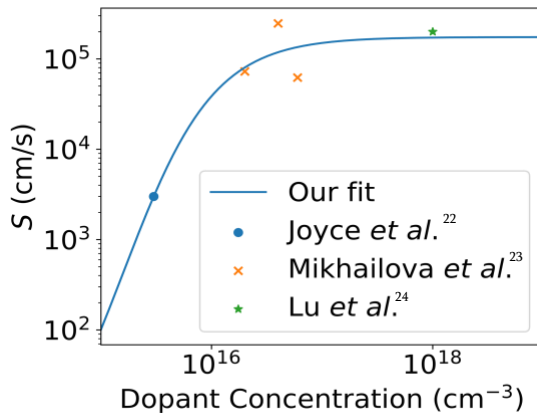


Figure S4. InAs surface recombination velocity as a function of doping concentration, together with the model fitting obtained by this work. The experimental data are taken from Refs. 22,23 as well as from our best fit to the TPV cell from Lu et al.²⁴

6. Electrical model validation

To validate the electrical model, we compare measured and simulated dark current-voltage curves of devices from Refs. 24,25. Figure S5(a) shows the simulation structure for the device from Lu et al.²⁴, which we simulate as a 3D cylindrical device. We assumed the substrate thickness and doping to be 500 μm and $2 \times 10^{18}\text{ cm}^{-3}$, respectively, and extracted the contact width (20 μm) from Figure 1 within the article. Figure S5(c) shows the simulation structure for the device from Krier et al.²⁵. We assumed the substrate thickness to be 500 μm . We extracted the contact width (20 μm) and distance between contacts (75 μm) from Figure 2 within the article. The remaining parameters for both devices were taken from the text of the articles.

The fits to data from Ref. 24 and Ref. 25 are shown in Fig. Figure S5(b) and Fig. Figure S5(d), respectively. In our simulations, we added a resistor in series with the TPV cells to account for resistive losses arising from the electrode sheet and contact resistances. We allow the SRH recombination lifetime of InAs, the surface recombination velocity at the TPV cell surface, and the resistance of the resistor in series to vary to obtain a good fit. For the device from Krier et al.²⁵, we also included the Hurkx trap-assisted tunneling model to improve the fit at reverse bias. The model simulates field-dependent trap-assisted tunneling and requires a single extra parameter, a tunneling mass. As shown in Figure S5(d), the Hurkx model does not affect the properties of the current-voltage curve under forward bias and therefore does not affect the results in this manuscript. Results of the fits are shown in Table S4. **Error! Reference source not found..**

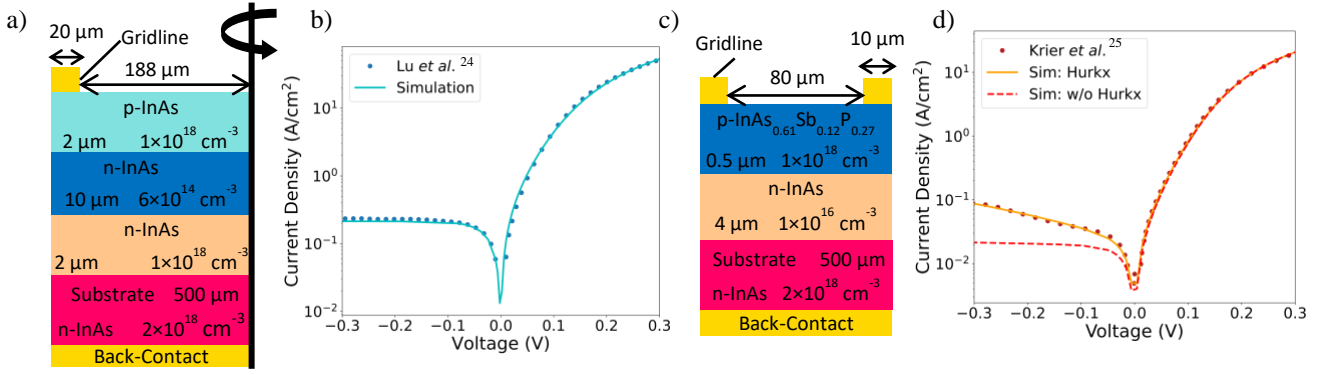


Figure S5. (a,c) Simulated device structure, and (b,d) dark current density as a function voltage plots, comparing our simulations to measurements for devices from Lu et al.²⁴ and Krier et al.²⁵, respectively. We assume TPV cell temperatures of 300 K.

Table S4. Parameter values after our fit to measured dark current-voltage data.

Parameters	Units	Lu et al. ²⁴	Krier et al. ²⁵
SRH lifetime	s	3.7×10^{-7}	2.7×10^{-7}
Series resistance	Ω	1.6	1.06
Surface recombination velocity	cm/s	2×10^5	2×10^5
Hurkx tunneling mass	m_0	-	7.5×10^{-4}

7. Cap and BSF Parameter Impact on Performance

We fixed the Cap and BSF layer thicknesses and doping during our optimization to help with computation time. To verify the robustness of our optimization results, we explore the impact of these parameters on the optimized nip-Q design, in Figure S6, for a 750 K radiator and $d_{R-FSF} = 0.1 \mu\text{m}$. In general, the device efficiency is maximized with highly doped Cap and BSF layers as they maximize the built-in electric field. For the cap layer (Figure S6(a)), we calculate maximized efficiency if doping concentration is above $3 \times 10^{18} \text{ cm}^{-3}$, irrespective of layer thickness. Conversely, device efficiency is strongly affected by the BSF layer thickness, see Figure S6(b). We require a thickness less than $0.08 \mu\text{m}$ to stay within 1% absolute of the maximal efficiency, due to higher sub-bandgap photon absorption for thicker layers.

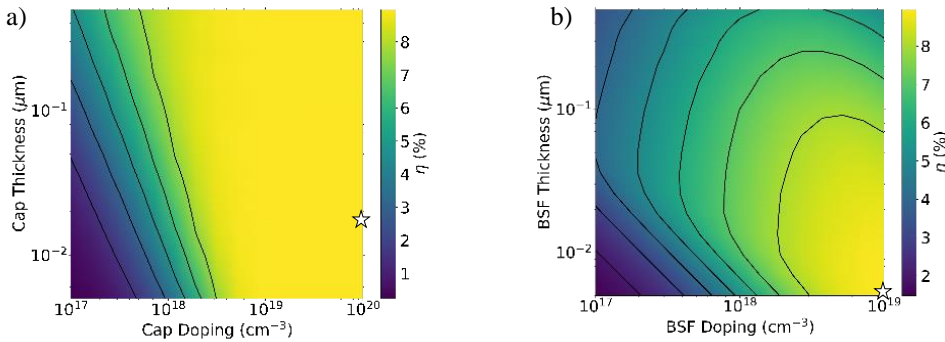


Figure S6. Device efficiency for a 750 K radiator and $d_{R-FSF} = 0.1 \mu\text{m}$ for the optimized nip-Q device, as a function of layer thickness and doping for the (a) Cap layer and (b) BSF layer. Stars depict parameters used for device optimization of the nip-Q design.

References

- ¹ M. Sotoodeh, A.H. Khalid, and A.A. Rezazadeh, J. Appl. Phys. **87**, 2890 (2000).
- ² X. Peng, B. Zhang, G. Li, J. Zou, Z. Zhu, Z. Cai, S. Zhou, Y. Li, Z. Wang, and W. Jiang, Infrared Phys. Technol. **54**, 454 (2011).

- ³ H.H. Wieder, Appl. Phys. Lett **25**, 206 (1974).
- ⁴ M. Levinshtein, S. Rumyantsev, and M. Shur, *Handbook Series on Semiconductor Parameters, Vol. 1* (1996).
- ⁵ Y. Lin, A.R. Arehart, and A.M. Carlin, Appl. Phys. Lett **93**, 62109 (2008).
- ⁶ R.T. Hinkey, Z. Tian, and R.Q. Yang, J. Appl. Phys **110**, 43113 (2011).
- ⁷ S. Law, D.C. Adams, A.M. Taylor, and D. Wasserman, (2012).
- ⁸ D. Wei, S. Maddox, P. Sohr, S. Bank, S. Bank, S. Law, and S. Law, Opt. Mater. Express, Vol. 10, Issue 2, Pp. 302-311 **10**, 302 (2020).
- ⁹ S. Adachi, *Properties of Semiconductor Alloys: Group-IV, III-V and II-VI Semiconductors* (John Wiley & Sons, LTD., 2009).
- ¹⁰ M.Y. Swinkels, M.R. Van Delft, D.S. Oliveira, A. Cavalli, I. Zardo, R.W. Van Der Heijden, and A.M. Bakkers, (2015).
- ¹¹ R. Mittapally, B. Lee, L. Zhu, A. Reihani, J.W. Lim, D. Fan, S.R. Forrest, P. Reddy, and E. Meyhofer, Nat. Commun. 2021 121 **12**, 1 (2021).
- ¹² C.J. Fu and Z.M. Zhang, Int. J. Heat Mass Transf. **49**, 1703 (2006).
- ¹³ S. Basu, B.J. Lee, and Z.M. Zhang, J. Heat Transfer **132**, 1 (2010).
- ¹⁴ V. Alex, S. Finkbeiner, and J. Weber, J. Appl. Phys. **79**, 6943 (1996).
- ¹⁵ A. Derkachova, K. Kolwas, and I. Demchenko, Plasmonics **11**, 941 (2016).
- ¹⁶ S. Adachi, *Optical Properties of Crystalline and Amorphous Semiconductors: Materials and Fundamental Principles* (Kluwer Academic Publishers, 1999).
- ¹⁷ D. Milovich, J. Villa, E. Antolin, A. Datas, A. Marti, R. Vaillon, and M. Francoeur, J. Photonics Energy **10**, 025503 (2020).
- ¹⁸ I. Vurgaftman, J.R. Meyer, and L.R. Ram-Mohan, J. Appl. Phys. **89**, 5815 (2001).
- ¹⁹ Y.B. Li, R.A. Stradling, T. Knight, J.R. Birch, R.H. Thomas, C.C. Phillips, and I.T. Ferguson, Semicond. Sci. Technol. **8**, 101 (1993).
- ²⁰ S. Adachi, *Properties of Group-IV, III-V and II-VI Semiconductors* (Wiley Blackwell, 2005).
- ²¹ H. Ito and T. Ishibashi, Jpn. J. Appl. Phys. **33**, 88 (1994).
- ²² H.J. Joyce, C.J. Docherty, Q. Gao, H.H. Tan, C. Jagadish, J. Lloyd-Hughes, L.M. Herz, and M.B. Johnston, Nanotechnology **24**, (2013).
- ²³ M.P. Mikhailova, D.N. Nasledov, and S. V. Slobodchikov, Phys. Status Solidi **11**, 529 (1965).
- ²⁴ Q. Lu, X. Zhou, A. Krysa, A. Marshall, P. Carrington, C.H. Tan, and A. Krier, Sol. Energy Mater. Sol. Cells **179**, 334 (2018).
- ²⁵ A. Krier, M. Yin, A.R.J.J. Marshall, and S.E. Krier, J. Electron. Mater. **45**, 2826 (2016).